**Part I**
**Basics and Methods**

# 1
# Introduction to Scanning Electron Microscopy

*Christina Scheu and Wayne D. Kaplan*

The scanning electron microscope is without doubt one of the most widely used characterization tools available to materials scientists and materials engineers. Today, modern instruments achieve amazing levels of resolution, and can be equipped with various accessories that provide information on local chemistry and crystallography. These data, together with the morphological information derived from the sample, are important when characterizing the microstructure of materials used in a wide number of applications. A schematic overview of the signals that are generated when an electron beam interacts with a solid sample, and which are used in the scanning electron microscope for microstructural characterization, is shown in Figure 1.1. The most frequently detected signals are high-energy backscattered electrons, low-energy secondary electrons and X-rays, while less common signals include Auger electrons, cathodoluminescence, and measurements of beam-induced current. The origin of these signals will be discussed in detail later in the chapter.

Due to the mechanisms by which the image is formed in the scanning electron microscope, the micrographs acquired often *appear* to be directly interpretable; that is, the contrast in the image is often directly associated with the microstructural features of the sample. Unfortunately, however, this may often lead to gross errors in the measurement of microstructural features, and in the interpretation of the microstructure of a material. At the same time, the fundamental mechanisms by which the images are formed in the scanning electron microscope are reasonably straightforward, and a little effort from the materials scientist or engineer in correlating the microstructural features detected by the imaging mechanisms makes the technique of scanning electron microscopy (SEM) being extremely powerful.

Unlike conventional optical microscopy or conventional transmission electron microscopy (TEM), in SEM a focused beam of electrons is rastered across the specimen, and the signals emitted from the specimen are collected as a function of position of the incident focused electron beam. As such, the final image is collected in a sequential manner across the surface of the sample. As the image in SEM is formed from signals emitted due to the interaction of a focused incident electron probe with the sample, two critical issues are involved in understanding SEM images, as well as in the correlated analytical techniques: (i) the nature of the incident electron probe; and (ii) the manner by which incident electrons interact with matter.
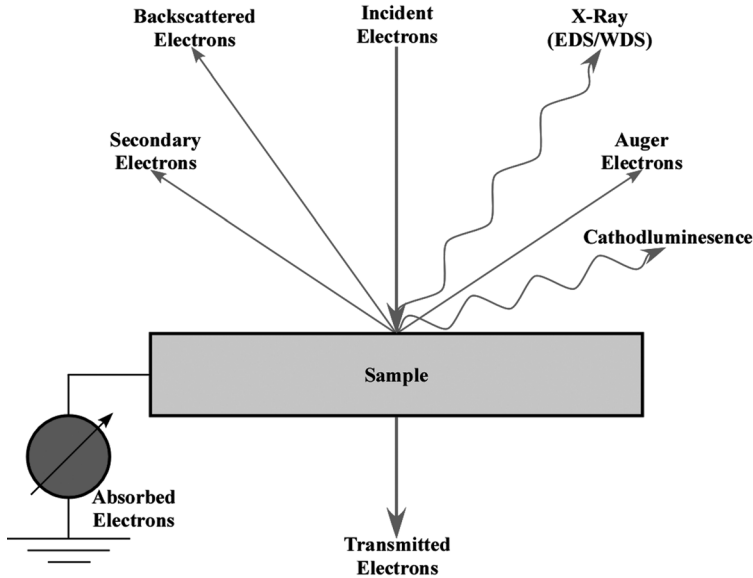
**Figure 1.1**  Schematic drawing of possible signals created when an incident electron beam interacts with a solid sample. Reproduced with permission from Ref. [4]; © 2008, John Wiley & Sons.

The electron–optical system in a scanning electron microscope is actually designed to demagnify rather than to magnify, in order to form the small incident electron probe which is then rastered across the specimen. As such, the size of the incident probe depends on the electron source (or gun), and the electromagnetic lens system which focuses the emitted electrons into a fine beam that then interacts with the sample. The probe size is the first parameter involved in defining the spatial resolution of the image, or of the analytical measurements. However, the signals (e.g., secondary electrons, backscattered electrons, X-rays) that are used to form the image emanate from regions in the sample that may be significantly larger than the diameter of the incident electron beam. Thus, electron–matter interaction must be understood, together with the diameter of the incident electron probe, to understand both the resolution and the contrast in the acquired image.

The aim of this chapter is to provide a fundamental introduction to SEM and its associated analytical techniques (further details are available in Refs [1–5]).

## 1.1
## Components of the Scanning Electron Microscope

It is convenient to consider the major components of a scanning electron microscope as divided into four major sections (see Figure 1.2):

- The electron source (or electron gun).

- The electromagnetic lenses, which are used to focus the electron beam and demagnify it into a small electron probe.
- The deflection system.
- The detectors, which are used to collect signals emitted from the sample.

Before discussing these major components, a few words should be mentioned regarding the vacuum system. Within the microscope, different levels of vacuum are required for three main reasons. First, the electron source must be protected against
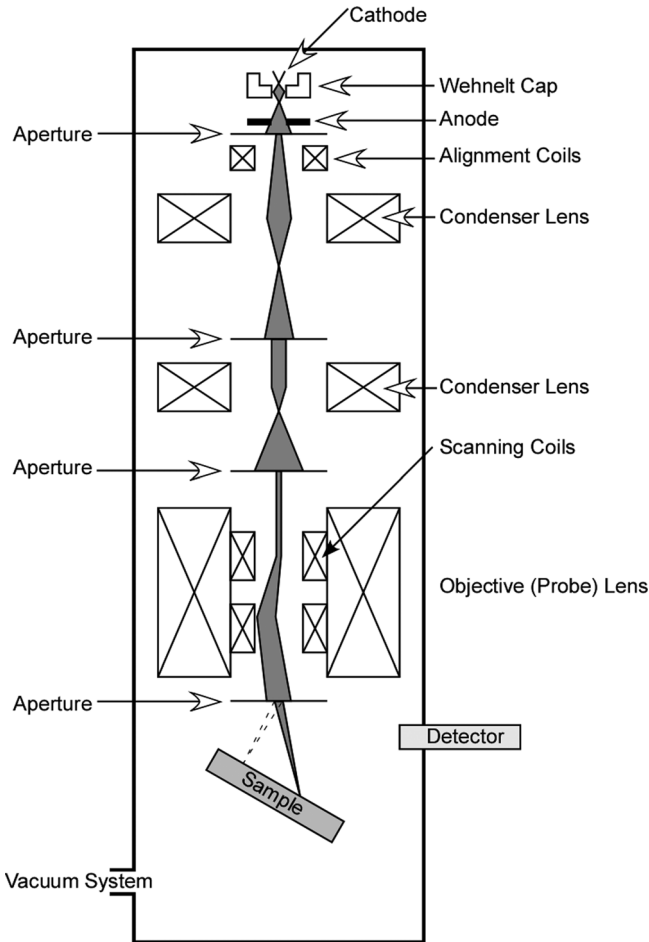


**Figure 1.2**   Schematic drawing of the major components of a scanning electron microscope. The electron lenses and apertures are used to demagnify the electron beam that is emitted from the electron source into a small probe, and to control the beam current density. The demagnified beam is than scanned across the sample. Various detectors are used to register the signals arising from various electron–matter interactions.

oxidation, which would limit the lifetime of the gun and may cause instabilities in the intensity of the emitted electrons. Second, a high level of vacuum is required to prevent the scattering of electrons as they traverse the column from the gun to the specimen. Third, it is important to reduce the partial pressure of water and carbon in the vicinity of the sample, as any interaction of the incident electron beam with such molecules on the surface of the sample may lead to the formation of what is commonly termed a "carbonaceous" (or contamination) layer, which can obscure the sample itself. The prevention of carbonaceous layer formation depends both on the partial pressure of water and carbon in the vacuum near the sample, and the amount of carbon and water molecules that are adsorbed onto the surface of the sample prior to its introduction into the microscope. Thus, while a minimum level of vacuum is always required to prevent the scattering of electrons by molecules (the concentration of which in the vacuum is determined from a measure of partial pressure), it is the partial pressure of oxygen in the region of the electron gun, and the partial pressure of carbon and water in the region of the specimen, that are in fact critical to operation of the microscope. Unfortunately, most scanning electron microscopes do not provide such measures of partial pressure, but rather maintain different levels of vacuum in the different regions of the instrument. Normally, the highest vacuum (i.e., the lowest pressure) is in the vicinity of the electron gun and, depending on the type of electron source, an ultra-high-vacuum (UHV) level (pressure $<10^{-8}$ Pa) may be attained. The nominal pressure in the vicinity of the specimen is normally in the range of $10^{-3}$ Pa. Some scanning electron microscopes that have been designed for the characterization of low-vapor pressure liquids, "moist" biological specimens or nonconducting materials, have differential apertures between the regions of the microscope. This allows a base vacuum as high as approximately 0.3 Pa close to the sample. These instruments, which are often referred to as "environmental" scanning electron microscopes, offer unique possibilities, but their detailed description is beyond the scope of the present chapter.

### 1.1.1
### Electron Guns

The role of the electron gun is to produce a high-intensity source of electrons which can be focused into a fine electron beam. In principle, free electrons can be generated by thermal emission or field emission from a metal surface (Figure 1.3). In thermal emission, the energy necessary to overcome the work function is supplied by heating the tip. In order to reduce the work function an electric field is applied ("Schottky effect"). If the electric field is of the order of 10 V nm$^{-1}$, the height and width of the potential barrier is strongly reduced, such that the electrons may leave the metal via field emission.

Although several different electron sources have been developed, their basic design is rather similar (see Figure 1.4). In a *thermionic source*, the electrons are extracted from a heated filament at a low bias voltage that is applied between the source and a cylindrical cap (the Wehnelt cylinder). This beam of thermionic
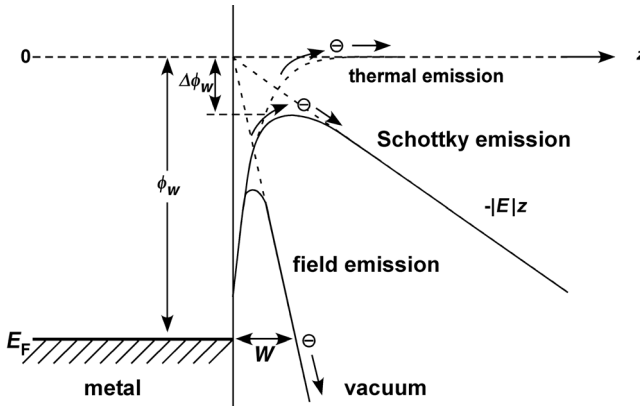
**Figure 1.3** Schematic drawing of the electrostatic potential barrier at a metal surface. In order to remove an electron from the metal surface, the work function must be overcome. The work function can be lowered by applying an electric field (Schottky effect). If the field is very high, the electrons can tunnel through the potential barrier. Redrawn from Ref. [1].

electrons is brought to a focus by the electrostatic field and then accelerated by an anode beneath the Wehnelt cylinder.

The beam that enters the microscope column is characterized by the effective source size $d_{gun}$, the divergence angle of the beam $\alpha_0$, the energy of the electrons $E_0$, and the energy spread of the electron beam $\Delta E$.

An important quantity here is the axial gun brightness ($\beta$), which is defined as the current $\Delta I$ passing through an area $\Delta S$ into a solid angle $\Delta \Omega = \pi \alpha^2$, where $\alpha$ is the angular spread of the electrons. With $j = \Delta I / \Delta S$ being the current density in A cm$^{-2}$, the following is obtained:

$$\beta = \frac{\Delta I}{\Delta S \Delta \Omega} = \frac{j}{\pi \alpha^2} = \text{const.} \tag{1.1}$$

The brightness is a conserved quantity, which means that its value is the same for all points along the optical axis, independent of which apertures are inserted, or how many lenses are present.

Currently, three different types of electron sources are in common use (Figure 1.4); the characteristics of these are summarized in Table 1.1. A heated tungsten filament is capable of generating a brightness of the order of $10^4$ A cm$^{-2}$ sr$^{-1}$, from an effective source size, defined by the first cross-over of the electron beam, approximately 15 µm across. The thermionic emission temperatures are high, which explains the selection of tungsten as the filament material. A lanthanum hexaboride LaB$_6$ crystal can generate a brightness of about $10^5$ A cm$^{-2}$ sr$^{-1}$, but this requires a significantly higher vacuum level in the vicinity of the source, and is now infrequently used in SEM instruments. The limited effective source size of thermionic electron guns, which must be demagnified by the electromagnetic lens system before impinging on the sample, leads to microscopes equipped with thermionic sources being defined as *conventional* scanning electron microscopes.
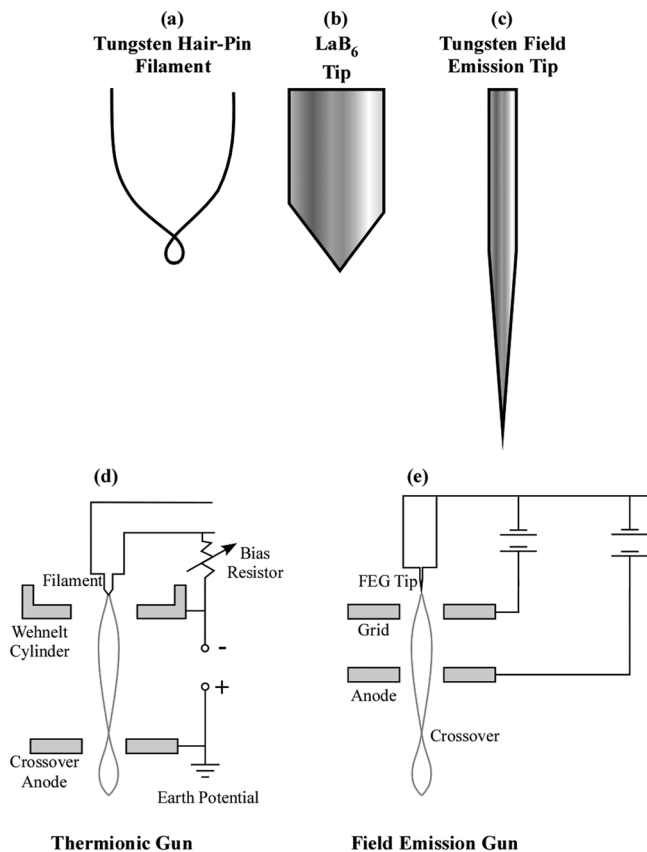
**Figure 1.4** Schematic drawings of (a) a tungsten filament and (b) a LaB$_6$ tip for thermionic electron sources. (c) For a field-emission gun (FEG) source, a sharp tungsten tip is used. (d) In thermionic sources the filament or tip is heated to eject electrons, which are then focused with an electrostatic lens (the Wehnelt cylinder). (e) In FEGs, the electrons are extracted by a high electric field applied to the sharp tip by a counterelectrode aperture, and then focused by an anode to image the source. Reproduced with permission from Ref. [4]; © 2008, John Wiley & Sons.

The effective source size can be significantly reduced (leading to the term *high-resolution* SEM) by using a "cold" field emission gun (FEG), in which the electrons "tunnel" out of a sharp tip under the influence of a high electric field (Figures 1.3 and 1.4). Cold FEG sources can generate a brightness of the order of $10^7$ A cm$^{-2}$ sr$^{-1}$, and the sharp tip of the tungsten needle that emits the electrons is of the order of 0.2 µm in diameter; hence, the effective source size is less than 5 nm. More often, a "hot" source replaces the "cold" source, in which case a sharp tungsten needle is heated to enhance the emission (this is termed a "thermal" field emitter, or TFE). The heating of the tip leads to a self-cleaning process; this has proved to be another benefit of TFEs in that they can be operated at a lower vacuum level (higher pressures). In the

**Table 1.1** A comparison of the properties of different electron sources.

| Source type | Thermionic | Thermionic | Schottky | Cold FEG |
|---|---|---|---|---|
| Cathode material | W | LaB$_6$ | W(100) + ZrO | W(310) |
| Work function [eV] | 4.5 | 2.7 | 2.7 | 4.5 |
| Tip radius [μm] | 50–100 | 10–20 | 0.5–1 | <0.1 |
| Operating temperature [K] | 2800 | 1900 | 1800 | 300 |
| Emission current density [A cm$^{-2}$] | 1–3 | 20–50 | 500–5000 | 104–106 |
| Total emission current [μA] | 200 | 80 | 200 | 5 |
| Maximum probe current [nA] | 1000 | 1000 | >20 | 0.2 |
| Normalized brightness [A cm$^{-2}$ sr$^{-1}$] | 104 | 105 | 107 | 2 × 107 |
| Energy spread at gun exit [eV] | 1.5–2.5 | 1.3–2.5 | 0.4–0.7 | 0.3–0.7 |

so-called "Schottky emitters," the electrostatic field is mainly used to reduce the work function, such that electrons leave the tip via thermal emission (see Figure 1.3). A zirconium-coated tip is often used to reduce the work function even further. Although Schottky emitters have a slightly larger effective source size than cold field emission sources, they are more stable and require less stringent vacuum requirements than cold FEG sources. Equally important, the probe current at the specimen is significantly larger than for cold FEG sources; this is important for other analytical techniques used with SEM, such as energy dispersive X-ray spectroscopy (EDS).

## 1.1.2
### Electromagnetic Lenses

Within the scanning electron microscope, the role of the general lens system is to demagnify an image of the initial crossover of the electron probe to the final size of the electron probe on the sample surface (1–50 nm), and to raster the probe across the surface of the specimen. As a rule, this system provides demagnifications in the range of 1000- to 10 000-fold. Since one is dealing with electrons rather than photons the lenses may be either electrostatic or electromagnetic. The simplest example of these is the electrostatic lens that is used in the electron gun.

Electromagnetic lenses are more commonly encountered, and consist of a large number of turns of a copper wire wound around an iron core (the pole-piece). A small gap located at the center of the core separates the upper and lower pole-pieces. The magnetic flux of the lens is concentrated within a small volume by the pole-pieces, and the stray field at the gap forms the magnetic field. The magnetic field distribution is inhomogeneous in order to focus electrons traveling parallel to the optical axis onto a point on the optical axis; otherwise, they would be unaffected. Thereby, the radial component of the field will force these electrons to change their direction in such a way that they possess a velocity component normal to the optical axis; the longitudinal component of the field would then force them towards the optical axis. Accordingly, the electrons move within the lens along screw trajectories about the optical axis due

to the Lorentz force associated with the longitudinal and radial magnetic field components.

Generally, in order to determine the image position and magnification (demagnification) for the given position of the object, it is possible to use the lens formula:

$$\frac{1}{F} = \frac{1}{U} + \frac{1}{V} \tag{1.2}$$

where $F$ is the focal length of the lens, $U$ is the distance between the object and the lens, and $V$ is the distance between the image and the lens. The magnification (demagnification) of the image – that is, the ratio of the linear image size $h$ to the corresponding linear size of the object $H$ – is equal to (see Figure 1.5):

$$M = \frac{h}{H} = \frac{V}{U}. \tag{1.3}$$

If $U \gg F$, then for the total demagnification of a three-lens system a spot is obtained with a geometric diameter of

$$d_0 = \frac{F_1 F_2 F_3}{U_1 U_2 U_3} d_{gun} = M d_{gun} \tag{1.4}$$

where $d_{gun}$ is the initial crossover diameter. To obtain $d_0 \leq 10$ nm for a thermionic cathode, which possesses an initial crossover $d_{gun}$ of $\approx$20–50 μm, the total demagnification must be $\leq 1/5000$. A Schottky or field-emission gun can result in $d_{gun} \leq 10$ nm, such that only one probe-forming (objective) lens is necessary to demagnify the electron probe to $d_0 \approx 1$ nm. The distance between the objective lens and the sample surface is termed the "working distance" of the microscope. From the above discussion, it follows that a short working distance will lead to a stronger demagnification and thus to a smaller electron probe size.
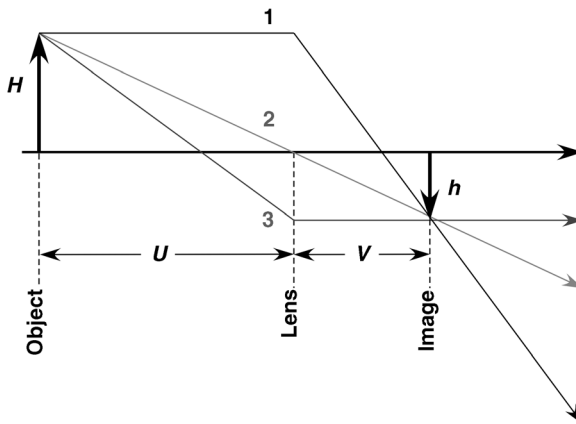


**Figure 1.5** Schematic drawing of the relationship between focal length and magnification for a ideal "thin" lens. Reproduced with permission from Ref. [4]; © 2008, John Wiley & Sons.

As with any lens system, the final size (and shape) of the electron probe will also depend on aberrations intrinsic to the electromagnetic lenses used in the scanning electron microscope. In a simplistic approach, the three main lens aberrations are spherical and chromatic aberrations (Figure 1.6) and astigmatism (Figure 1.7):

- *Spherical aberration* results in electrons traversing different radial distances in the lens ($r_1$ and $r_2$ in Figure 1.6a), to be focused at different focal lengths; this will result in a blurring of the image (and a finite resolution).
- Due to *chromatic aberrations*, electrons having a difference in energy (wavelength) are focused to different focal lengths along the optical column (Figure 1.6b). In contrast to optical microscopy, electrons with shorter wavelengths (i.e., higher energy) will reach a focal point at larger focal lengths.
- Finally, *astigmatism* results in different focal lengths for electrons entering the lens at different tangential angles about the optical axis (Figure 1.7).
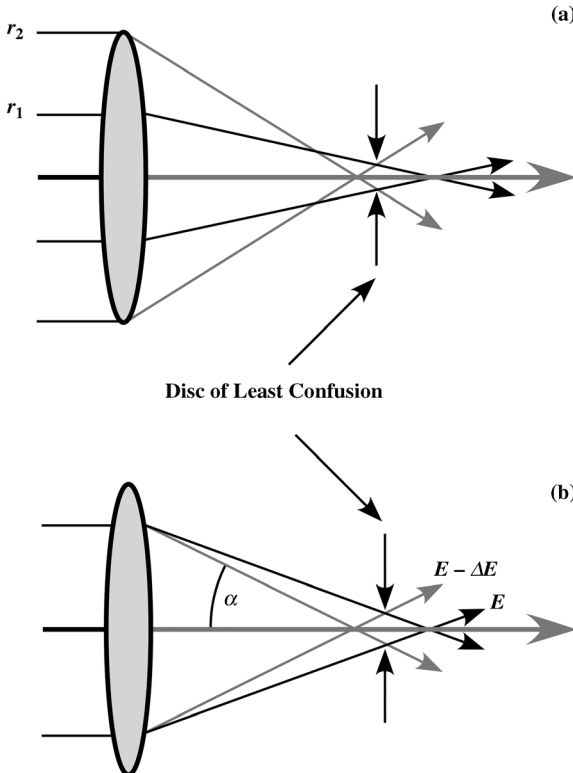


**Figure 1.6** (a, b) Schematic drawings of the influence of (a) spherical and (b) chromatic aberrations on the focused electron probe. In this schematic drawing the angles of deflection are exaggerated. Reproduced with permission from Ref. [4]; © 2008, John Wiley & Sons.
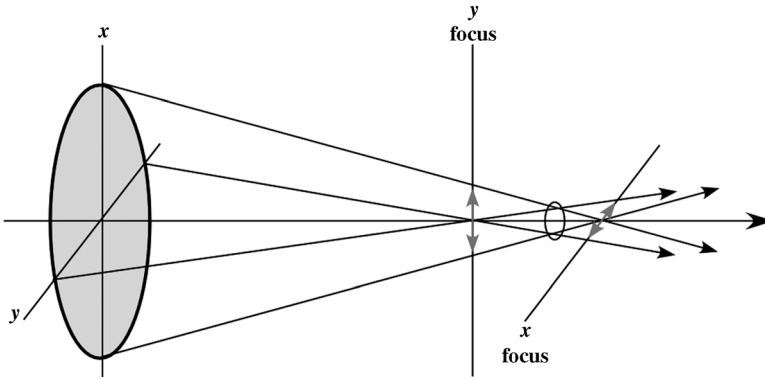
**Figure 1.7** Schematic drawing of the influence of astigmatism on size of a focused electron probe. Reproduced with permission from Ref. [4]; © 2008, John Wiley & Sons.

The electron current density $j_p$ and the probe aperture-dependent semi-convergence angle $\alpha_p$ are linked via the gun brightness, $\beta$:

$$j_p = \pi \beta \alpha_p^2. \tag{1.5}$$

If it is assumed, for simplicity, that the current density is uniform over a circle of diameter $d_0$, then the total probe current will be given by:

$$i_p = \frac{\pi}{4} d_0^2 j_p. \tag{1.6}$$

Then:

$$d_0 = \sqrt{\frac{4i_p}{\beta}} \cdot \frac{1}{\pi \alpha_p} = C_0 \frac{1}{\alpha_p}. \tag{1.7}$$

It is important to note that the parameters $i_P$, $d_0$ and $\alpha_P$ cannot be varied independently since, as mentioned above, the brightness remains constant. For a fixed vale of $d_0$ and $\alpha_P$, a large value of $\beta$ will be required to obtain a large probe current, $i_P$.

This geometric probe diameter $d_0$ is broadened by the action of the lens aberrations. Assuming a Gaussian distribution for both the geometric electron probe profile and all the aberrations, one obtains for the probe size:

$$d_p^2 = d_0^2 + d_d^2 + d_s^2 + d_c^2 \tag{1.8}$$

$$d_p^2 = \left[ C_0^2 + (0.6\lambda)^2 \right] \alpha_p^{-2} + 0.25 C_s^2 \alpha_p^6 + \left( C_c \frac{\Delta E}{E} \right)^2 \alpha_p^2 \tag{1.9}$$

where $C_0$ contains the probe current and the gun brightness, $d_d$ is the diffraction limit due to the apertures, and $C_S$ and $C_C$ are the spherical and chromatic aberration coefficients, respectively. When using a scanning electron microscope with a

thermionic cathode, the constant $C_0$ is much larger than $\lambda$, which means that the diffraction error can be neglected. The dominant terms are those containing $C_0$ and $C_S$ because, for energies in the 10 to 20 kV range, the term that contains $C_C$ becomes small due to the presence of $\Delta E/E$. When operating with $E < 5$ keV, the chromatic error term dominates and $C_0$ is increased owing to the decrease in $\beta$ (which is proportional to $E$).

### 1.1.3
### Deflection System

As mentioned above, the image is formed by scanning a focused electron beam along a raster where, at each point, a signal produced by the interaction between the incident electron beam and the sample is detected, amplified, and displayed. Scanning over a raster is accomplished by two pairs of scanning coils which deflect the electron beam along a line; the coils then move the beam to the beginning of the next line where it is again deflected. By repeating this process the entire rastered area can be scanned. Simultaneously, a spot is scanned over the viewing screen, and displays the detected signal at each point. The viewing screen is either a cathode ray tube (these are rarely used in modern systems) or a liquid crystal display (LCD) computer monitor-based system.

Due to the image formation process, the magnification $M$ of a scanning electron microscope is given by the ratio of the length of the raster on the viewing screen $L_{\text{Screen}}$ and the length of the raster on the sample surface $L_{\text{Sample}}$:

$$M = {L_{\text{Screen}}}\big/{L_{\text{Sample}}}. \tag{1.10}$$

### 1.1.4
### Electron Detectors

As will be described in detail later, electron–matter interaction can lead to the emission of secondary electrons (SEs) and backscattered electrons (BSEs). These are distinguished by their energy, with electrons having energies $<50$ eV being considered as SEs, while those with energies close to that of the incident electron beam are labeled BSEs. Both can be used in the imaging process in the scanning electron microscope, while several different types of detectors are required to differentiate between them.

#### 1.1.4.1 Everhart–Thornley Detector
One of the most frequently used detectors, the Everhart–Thornley (ET), can be used to detect both SEs and BSEs. The basic components of an ET detector (see Figure 1.8) include a scintillator which is surrounded by a metal collector grid, a light guide, and a photomultiplier system. Any electrons that enter the detector are collected if their energy is sufficient to create photons in the scintillator; the photons are then guided via a light guide to a photomultiplier system where the photon causes electrons to be
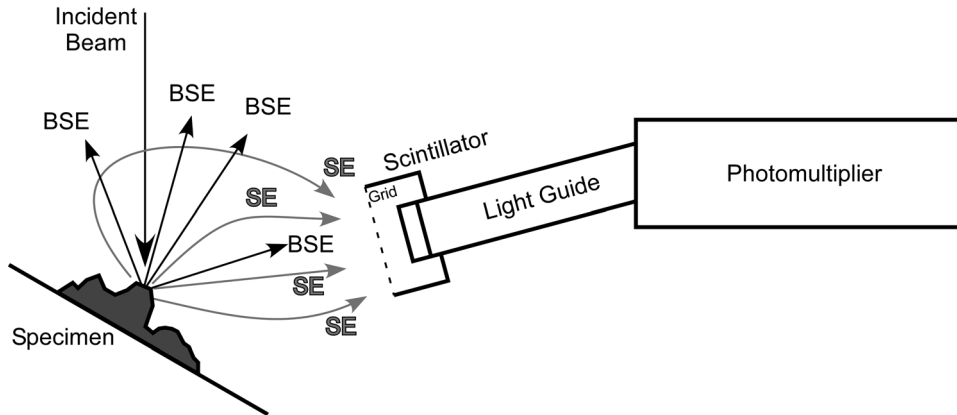
**Figure 1.8** Schematic drawing of an Everhart–Thornley (ET) detector. The scintillator is biased to attract the electrons, and a separate bias on the grid can be used to screen against low-energy SE electrons. Modified from Ref. [2].

ejected from a photocathode and accelerated to the first of a series of positively biased dynodes of the photomultiplier systems, where they cause further electrons to be ejected. These latter electrons, and also those originally impinging on the first dynode, are accelerated to subsequent dynodes where the process of electron ejection is repeated. In this way, a large amplification of the incoming signal is obtained, depending on the number of dynodes present and the voltage applied. At the last dynode, which serves as the anode, the incoming electron current pulse is converted to a voltage pulse, with the help of a resistor. The voltage pulse is then further amplified by an electronic system and used to generate the signal which, after conversion to a digital signal in the case of a modern scanning electron microscope, is displayed on the viewing screen. Consequently, the brightness of each image point (pixel) in the image will be directly related to the number of SEs or BSEs detected.

Although, the energy of a SE is not sufficient to create photons in the scintillator, this problem can be overcome by coating the scintillator with a thin, positively biased ($\sim$10 keV) aluminum film. This causes the incoming SE electrons to be accelerated to a value necessary to create photons. A biased ($-200$ to $+200$ V) metal collector grid is located immediately in front of the scintillator. If a positive bias is applied to the grid, then the SEs emitted from the sample in directions not towards the detector will be strongly attracted towards the metal grid, thus increasing the efficiency of collection. This also means that any BSEs traveling in the direction of the ET detector will always contribute to the signal (albeit to only a small degree). In order to obtain only the signal from the BSEs, either the metal collector grid must be negatively biased, or the voltage applied to the scintillator turned off. Generally, the ET detector can be used for rapid acquisition (i.e., fast scan rates), and is usually located at an angle inclined to the sample surface at one side, so that it has only a limited solid angle detection range. Nevertheless, this geometric arrangement leads we want this effect, it is not unfortunately to shadowing effects, and to a three-dimensional effect (3-D) in the final image (see below).

### 1.1.4.2 **Scintillator Detector**

It is worth mentioning that BSEs are only weakly deflected by the electrical field associated with the collector bias voltage of the ET detector, and that they basically move without being disturbed in the direction that they are emitted. Accordingly, as the detection efficiency for BSEs will be low for an ET detector, dedicated scintillator detectors for BSE detection have been developed which have a large solid angle of detection and an annular detection area which is located above the sample surface (Figure 1.9). In a manner similar to the ET detector, the BSEs first create photons in the scintillator; the photons are then guided to a photomultiplier system, where they produce photoelectrons which are further amplified. The annular detector has an opening in the center to allow the incident electron beam to reach the sample surface.
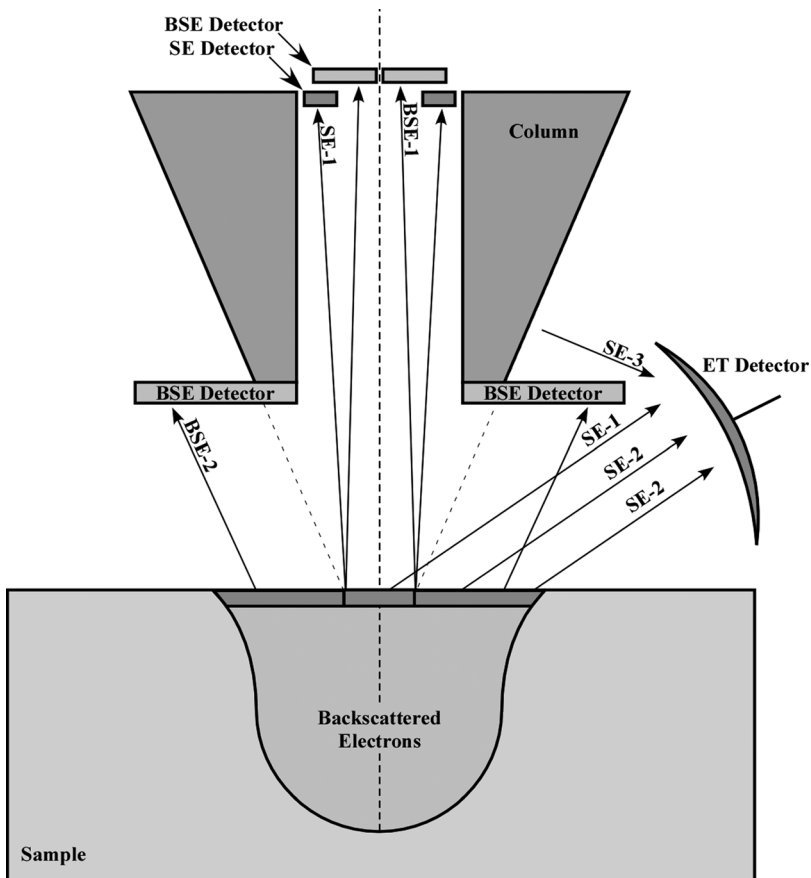


**Figure 1.9** Schematic drawing of an in-lens detector system, combined with a standard BSE and ET detector. The in-lens detectors are efficient only over small working distances, where the ET and conventional detectors have low detector efficiencies. Reproduced with permission from Ref. [4]; © 2008, John Wiley & Sons.

However, as the BSE scintillator detectors are usually rather thick in terms of their dimensions, they may limit the available working distance of the SEM.

### 1.1.4.3 Solid-State Detector

Another possible approach to detecting BSEs is the solid-state detector (Figure 1.9). In this case, the annular semiconductor detector is placed above the sample and has, again, a hole through which the incident electron beam can pass. The active area is often separated into different segments, from which the signal can be read out separately. A BSE that strikes the active area generates electron-hole pairs at the pn-junction of the detector, which is formed at the interface between p- and n-type doped Si. The electron and holes are separated in the electrical field of the space charge region; this leads to a current pulse which is transformed to a voltage pulse with the help of an external resistor. While solid-state detectors usually have slow acquisition rates compared to scintillators and ET detectors, their main advantage is that signals from the individual segments can be combined to obtain various contrast mechanisms. A second benefit is that they are rather thin in terms of their dimensions, which allows smaller working distances.

### 1.1.4.4 In-Lens or Through-the-Lens Detectors

As their name implies, "in-lens" or "through-the-lens" detectors are placed directly inside the SEM lens system (Figure 1.9). Those SEs that are emitted to a certain solid angular regime from the sample surface are subjected to the magnetic field of the lens pole piece and reach the detector which, again, is based on a scintillator-light guide-photomultiplier system. Any BSEs and SEs that are emitted at larger angles will not be detected. The spatial resolution obtained by using such an in-lens detector system is significantly improved compared to that of conventional detectors (down to <1 nm for SEs), as only those electrons emitted from a region that is directly defined by the incident beam size are collected.

## 1.2
## Electron–Matter Interaction

An incident electron beam that impinges on a sample surface can undergo both elastic and inelastic scattering events as it penetrates the solid sample. *Inelastic scattering* refers to any process in which the primary electron loses a detectable amount of energy $\Delta E$, whereas in *elastic scattering* the electron energy remains unchanged.

All backscattered electrons lose some energy during the scattering process. Although the analytical treatment of inelastic scattering is beyond the scope of this chapter, an outline will be provided of BSEs, following an elastic model. *Elastic scattering* occurs due to the coulombic interaction of the incident charged electron with the electrical field of the atomic nucleus, which is screened by the inner-shell electrons. This scattering process can be described as "Rutherford scattering" at a screened nucleus:

$$\frac{d\sigma}{d\Omega} \approx \frac{Z^2}{E_0^2 [\mathrm{Sin}^2(\theta/2) + \mathrm{Sin}^2(\theta_0/2)]^2} \qquad (1.11)$$

where $\frac{d\sigma}{d\Omega}$ is the differential cross-section which gives the probability that an electron is scattered into a solid angle element $d\Omega$, $\theta$ is the scattering angle, $\theta_0$ the characteristic angle or screening parameter which depends on the wavelength and the screening radius of the atom, $Z$ the atomic number, and $E_0$ is the incident beam energy. For large scattering angles, and in particular backscattering ($>90°$), Eq. 1.11 is not valid and the electron spin must be considered. This so-called "Mott scattering" leads to a more complicated mathematical description of the differential cross-section that is beyond the scope of this chapter. Nevertheless, for the most probable elastic scattering angles, which are between $3°$ and $5°$, the concept of Rutherford scattering from a screened nucleus can be used as an approximation. Multiple elastic scattering events can result in large scattering angles, and cause the electron trajectories to spread relative to the incident beam position. A cumulative change in direction may lead to electrons which finally can escape from the sample surface. These electrons, together with those that are directly scattered to angles $>90°$, are termed "backscattered" electrons and are used for imaging (as discussed below).

*Inelastic scattering* may occur as a result of several processes, including the excitation of phonons, plasmons, single-valence electrons, or inner-shell electrons (Figure 1.10). The average amount of energy that is transferred from the incident electron to the sample is different for these various events. For example, the excitation of phonons which are atomic vibrations in the solid are associated with an energy loss $\Delta E < 1$ eV, and lead to a slight heating of the sample, whereas the excitation of plasmons, which occurs via a collective excitation of the electron gas, is related to an energy loss of $\Delta E \approx$ 5–30 eV. Single-valence electron excitation requires an energy transfer of a few eV up to a few tens of eV. In order to excite the inner-shell electrons of the atoms, the incident electron must lose a larger amount of energy, typically in the range of hundreds to several thousands of eV. However, the probability that an electron loses a large quantity of its energy is low, and decreases rapidly with increasing energy loss. Consequently, processes which involve an energy transfer in the range of 5 to 50 eV dominate and, accordingly, the electrons lose their energy continuously in small quantities. The average inelastic mean free path (MFP), which describes the average distance that the
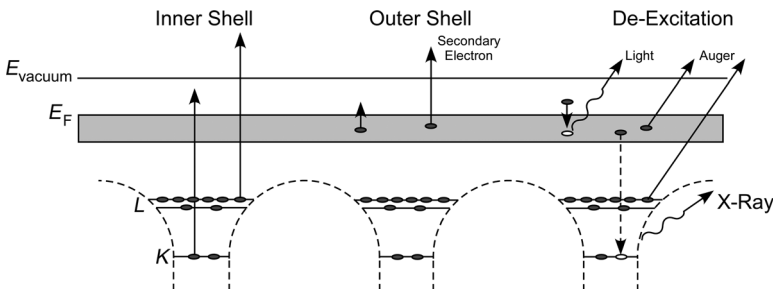


**Figure 1.10** Schematic drawing of an energy diagram of a solid. Possible primary and secondary effects are indicated. Redrawn from Ref. [6].

electron can travel before being inelastically scattered, depends on the specific sample material and the incident electron energy, but typically is of the order of 100 nm. The scattering angle for inelastic scattering is small (usually <1°).

Although all inelastic scattering events have a different differential cross-section which considers the underlying physics, the Bethe formula can be used as a first approximation to estimate the average energy loss $dE$ that occurs when the electron has traveled a distance $ds$ in the material:

$$\frac{dE}{ds} \approx \frac{Z\varrho}{AE_i} \ln\left(\frac{E_i}{I}\right) \tag{1.12}$$

where $Z$ is the atomic number, $\varrho$ the density, $A$ the atomic weight, $E_i$ the electron energy at point $i$ in the specimen, and $I$ the average energy loss per scattering event. The quantity $I$ is often estimated by an average ionization energy of the atom.

For thick samples, as are usually investigated using SEM, inelastic scattering processes dominate and the electron energy is reduced gradually. Due to multiple inelastic scattering processes, the electrons reach an average thermal kinetic energy of $kT$ (where $k$ is the Boltzmann constant and $T$ the temperature) and are finally absorbed in the sample. Therefore, most of the energy of the incident electron will result in heating of the sample, though a small quantity will be used to generate secondary electrons, X-rays, or light that, eventually, can escape from the solid (Figure 1.10). These effects are termed "secondary" as they can be detected outside the sample (these will be discussed further below).

Multiple elastic and inelastic scattering events result in a lateral and vertical spreading of the electron beam relative to the incident direction, and to a maximum distance which the electron can travel before it is absorbed ("penetration depth"). The associated volume, which is termed the "interaction volume," is typically pear-shaped in thick samples. The volume size is defined by an envelope which fulfills a specific condition; for example, the electron energy has been reduced to a specific value, or that the volume contains 95% of all incident electrons. The interaction volume may be calculated and visualized using Monte Carlo electron trajectory simulations, and various programs are available (e.g., Casino [7]). For these simulations, independent scattering centers are assumed within the solid where the electron can undergo either elastic or inelastic scattering in a random, statistical fashion. This is necessary to account for the large range of scattering angles and energy loss rates which are possible. Although Monte Carlo simulations usually ignore crystallo-graphic effects, they can provide very useful information on the general aspects of the interaction volume, such as its dependence on the incident beam energy and on the atomic number.

The influence of the incident beam energy on the size of the interaction volume is shown in Figure 1.11, where the interaction volume is larger for electrons with a higher energy; that is, with a higher acceleration voltage, both in the lateral and in the vertical directions. This can be explained with assistance from the above-described Rutherford and Bethe descriptions. Elastic scattering is inversely proportional to the square of the incident beam energy (Eq. 1.11); hence, with increasing beam energy
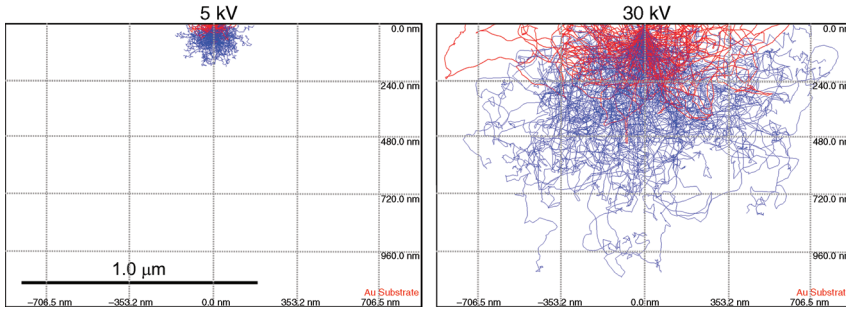
**Figure 1.11** Monte Carlo simulation of electron trajectories in Au, at an incident electron energy of 5 kV and 30 kV and using a 10 nm probe diameter. The red trajectories are for electrons which eventually escaped the sample. The scale bar is identical for both calculations. Calculated using CASINO [7].

the electrons are scattered less and can penetrate more deeply into the material. In addition, the average energy loss per distances traveled (Eq. 1.12) depends inversely on the beam energy. Accordingly, electrons with a higher energy can travel for a greater distance before being inelastically scattered and before (after multiple scattering) being absorbed by the sample.

The interaction volume also depends strongly on the atomic number $Z$, and its size is drastically reduced with increasing $Z$ (Figure 1.12). Besides this change in size, a change in shape is also observed, from pear-like to a more spherical shape with increasing atomic number. Again, this general trend may be better understood by
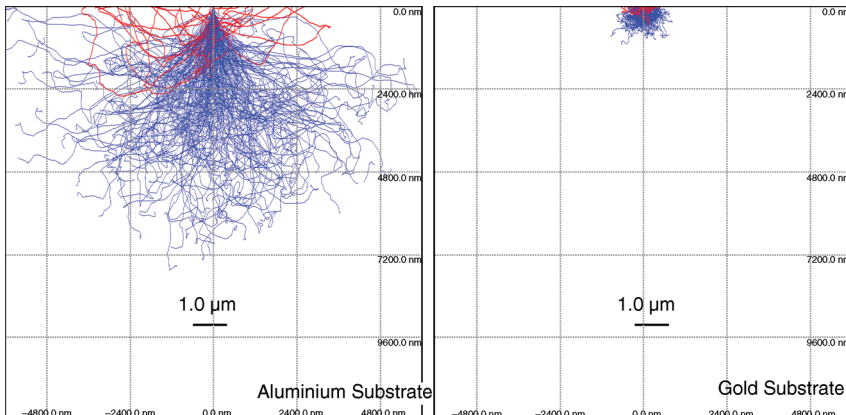


**Figure 1.12** Monte Carlo simulation of electron trajectories in Al and Au, at an incident electron energy of 30 kV and using a 10 nm probe diameter. The red trajectories are for electrons which eventually escaped the sample. Calculated using CASINO [7].
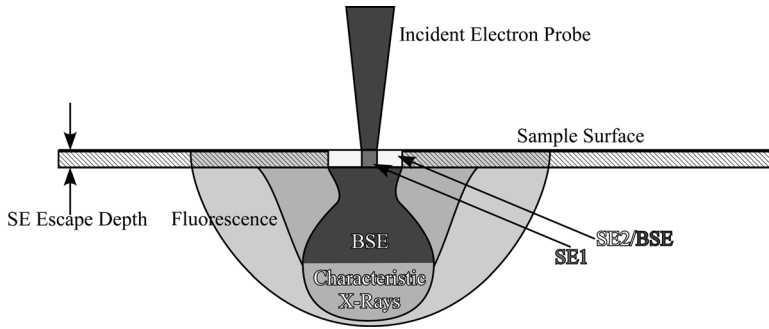
**Figure 1.13** Schematic drawing of the interaction volume for a given material and given energy of the incident beam electrons which, together with the escape depth, define the spatial resolution of each signal.

examining the probability for elastic scattering, which scales with the square of the atomic number (Eq. 1.11).

The critical finding from this discussion is that "*the interaction volume is much larger in dimensions compared to the incident beam diameter.*" Typical values for a 10 nm beam diameter can be lateral and vertical spread into a volume which has a length of 1 μm or more. This has a very strong impact on the spatial resolution of SEM, and for associated analytical techniques, as the various signals (SEs, BSEs, and X-rays) are generated within this interaction volume as long as the energy of the electrons is sufficient for the process. The interaction volume is a critical parameter for defining the spatial resolution which, for different imaging and spectroscopic techniques, is also governed by the *escape depth*. This is the maximum distance that the generated electrons or photons can travel (and leave the solid to reach the detector). As will be seen, the escape depth varies significantly for the different signals, and as such so does the corresponding spatial resolution (Figure 1.13).

### 1.2.1
### Backscattered Electrons (BSEs)

After a brief introduction to elastic and inelastic scattering effects, and the correlated interaction volume, it is now possible to discuss the secondary effects. First, the characteristics of BSEs will be described, followed by an explanation of the generation of SEs and Auger electrons. Finally, the basics regarding photon emission will be discussed.

As noted above, all electrons that leave the surface with energies >50 eV are termed BSEs. The contribution of the BSEs to the energy distribution of all electrons emitted from the sample surface forms a continuum with a large peak centered near $E_0$ (the energy of the primary beam) and a tail towards lower energies (Figure 1.14). The peak near $E_0$ possesses a higher intensity and smaller width for heavier elements compared to elements with a low atomic number. The BSEs are primary electrons (PEs) that originate in the incident electron beam, and are scattered in the reverse
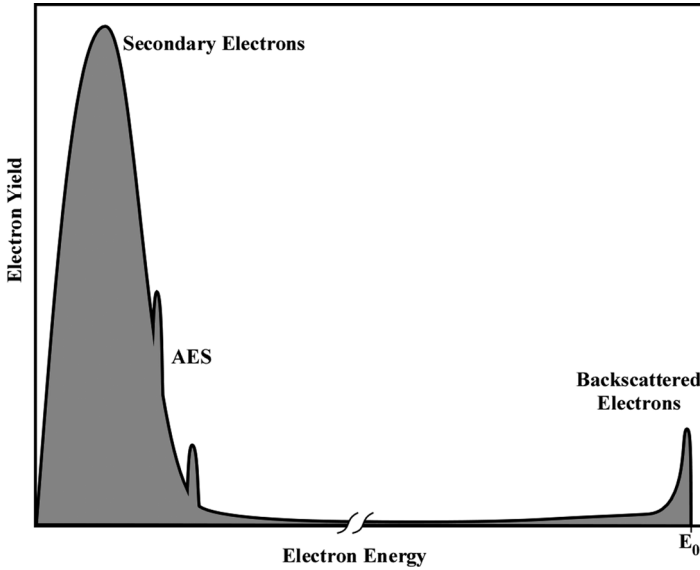
**Figure 1.14**  Energy distribution of electrons emitted from the sample surface. Reproduced with permission from Ref. [4]; © 2008, John Wiley & Sons.

direction (deflected by $>90°$), either by a single scattering event or, more likely, by multiple scattering events. The efficiency $\eta$ of BSE generation is defined as:

$$\eta \approx \frac{n_{BSE}}{n_{PE}} \tag{1.13}$$

where $n_{BSE}$ and $n_{PE}$ are the numbers of BSEs and PEs, respectively. The efficiency depends greatly on the atomic number $Z$ and the tilt angle $\theta$ of the incident beam direction relative to the sample normal. The detector position relative to the incident beam direction is also important.

The atomic number dependency shows a monotonic increase of $\eta$ with increasing $Z$ (Figure 1.15), giving rise to the so-called "atomic number contrast" or "compositional contrast." The efficiency also depends heavily on the tilt angle $\theta$; with an increasing tilt angle the efficiency ($\eta$) increases monotonically as more electrons can escape from the sample surface. It is this dependency on tilt angle that gives rise to a topological contrast in the BSE images. The effect of the incident beam energy on $\eta$ is much less pronounced. For incident beam energies $>5\,keV$, $\eta$ is basically independent of the beam energy, whereas for lower beam energies a weak dependence occurs. Such dependence is often obscured, however, by contamination layers which prevent successful BSE image acquisition in the low-energy regime.

At this point, it should be mentioned again that BSEs continue to travel along nearly straight trajectories in the direction that they are emitted, even when a collector bias voltage is applied, as the bias is often too weak to have any significant effect on the
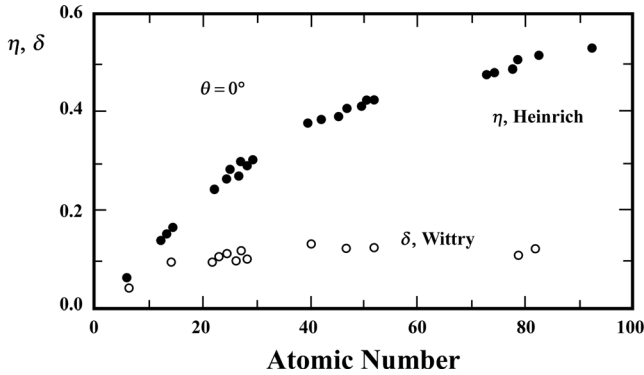
**Figure 1.15** Schematic drawing of the efficiency of BSE ($\eta$, after Heinrich, 1966) and SE ($\delta$, after Wittry, 1966) generation as a function of atomic number ($Z$) at an incident beam energy of 30 keV. Reproduced with permission from Ref. [3].

BSEs' trajectory. For image interpretation this directionality of motion is important, and the detector position relative to the BSEs' trajectories when they leave the sample must be considered. In fact, two cases should be distinguished: (i) when the incident beam direction is parallel to the surface normal; and (ii) when the incident beam direction possesses an angle relative to the surface normal. In the first case ($\theta = 0°$), $\eta$ follows a cosine function, being largest when the detector is placed parallel to the incident beam direction:

$$\eta(\phi) = \eta_n \cos \phi. \tag{1.14}$$

Here, $\eta_n$ is the value measured when the detector is placed parallel to the incident beam direction, and $\phi$ is the angle between the sample normal vector and the direction of the detector axis. Equation 1.14 implies that the signal decreases when $\phi$ is increased, reaching approximately 70% of $\eta_n$ for $\phi = 45°$. In the second case, and if $\theta$ is larger than ~45°, the angular distribution changes from a symmetrical cosine function to an asymmetric ellipsoidal distribution, such that backscattering is favored in directions away from the incident beam direction, and is highest in the forward direction. Thereby, the long axis of the ellipsoid is approximately at $(90° - \theta)$ above the sample surface as the incident beam. This dependency on the detector position also contributes to topological contrast in BSE images.

It is also important to note that the escape depth of BSEs can be in the range of microns, depending of course on their energy (see Figure 1.13). In addition, the interaction volume becomes asymmetric when $\theta$ is larger than 45°.

## 1.2.2
### Secondary Electrons (SEs)

As noted above, all electrons with energies between 1 eV and ~50 eV are termed SEs. The secondary electron yield $\delta$ is defined as the number of SE ($n_{SE}$) released per number of incident high-energy electrons ($n_{PE}$):

$$\delta = \frac{n_{SE}}{n_{PE}}. \tag{1.14}$$

It is important to remember that, in this equation, $n_{PE}$ *includes* the contribution from backscattered electrons which are traversing the solid and continue to generate SEs when they interact inelastically with the sample. As such, the SE yield is much higher than unity (typically >100%), and consequently most of the electrons detected are SEs. The secondary electron energy distribution shows a very large peak which is centered around 2–5 eV; this means that 90% of all detected SEs have an energy less than 10 eV (Figure 1.14). It is useful here to distinguish between two different types of SE, as they stem from different regions. The SE1 electrons are the outer-shell electrons of the sample that are directly excited by the incident beam electrons as they enter the surface and are able to escape (Figure 1.13). This is only possible if the SE1 electrons are excited above the vacuum level and are close to the sample surface. Their signal originates from an area which is approximately the diameter of the incident electron beam, and may be just under 1 nm. The SE2 electrons are generated by backscattered electrons after several inelastic scattering events. Consequently, the resolution of images formed by SE2 electrons is much worse than that of SE1 electrons, as the range of the backscattered electrons laterally across the sample may be on the order of microns (Figure 1.13). The advantage of "in-lens" detectors is now obvious, as most of the SE2 electrons are removed from the signal, such that the image is formed primarily from SE1 electrons.

The secondary electron yield $\delta$ depends on the incident beam energy, the work function of the surface, the incident beam angle relative to the sample normal (specimen tilt), and the local curvature of the sample. The dependency of the secondary electron yield $\delta$ on the incident beam energy $E_0$ is shown in Figure 1.16. For low incident beam energies, $\delta$ first increases to reach a maximum (at about 1 to 5 keV, depending on the material); above this value, $\delta$ slowly decreases with increasing $E_0$. The reason for this behavior can be explained as follows. For higher-keV incident electrons, the SEs are generated at a greater depth and thus cannot escape from the surface, whereas for lower-keV primary electrons the SEs are created closer to the sample surface, which makes it easier for them to escape. The incident beam energy has also another effect on $\delta$; with increasing beam energy, the brightness – and thus the incident beam current $i_P$ – is increased, which in turn leads to a higher SE current.

In general, the SE yield depends on the work function of the material, which is the energy barrier that an electron at the Fermi level must overcome to reach the vacuum level. The work function is of the order of a few eV, and depends on the material composition and the atomic packing at the surface – that is, the crystal structure and orientation. However, this dependency is usually obscured by contamination layers or any conductive layers (Au or C) deposited to prevent charging.

The atomic number $Z$ also influences the SE yield since, with increasing $Z$, a larger number of electrons will be backscattered and this will lead to a greater number of SEs. In addition, for samples with a higher mean $Z$, a larger percentage of SEs will be created near the surface, which will result in a greater probability of their escape
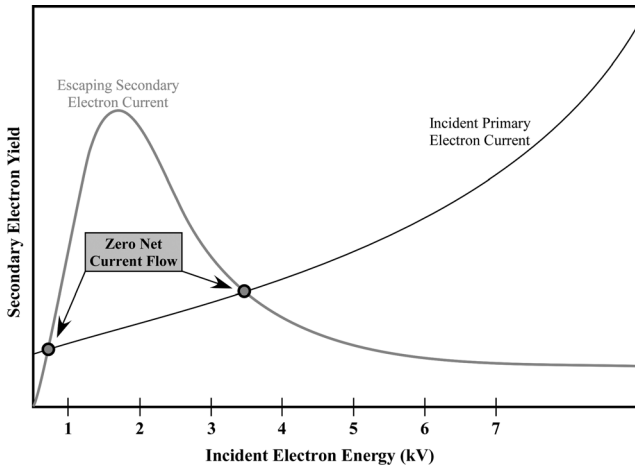
**Figure 1.16** Secondary electron yield (black curve) and incident primary electron current (gray curve) as a function of incident beam energy. Electrostatic charging of the sample is prevented at two points, which are marked by circles. At these points the total net current is zero. Reproduced with permission from Ref. [4]; © 2008, John Wiley & Sons.

(to reach the detector). This dependency on *Z* is higher for low incident beam energies where the escape depth of the SEs is of the order of the penetration depth of the incident beam electrons. For high accelerating voltages and non-UHV conditions, $\delta$ is often found to be relatively independent of the atomic number, which is again attributed to the fact that contamination or deposited conductive layers may obscure this effect. Nevertheless, the secondary electron yield $\delta$ is less strongly affected by *Z* compared to the efficiency $\eta$ of BSE generation, making the *Z* dependency in the SE images less pronounced (Figure 1.15).

The secondary electron yield $\delta$ is dependent on the angle $\theta$ of the incident beam relative to the sample normal. With increasing tilt angle, $\delta$ is increased and follows a sectant function:

$$\delta(\theta) = \delta_0 \sec \theta \tag{1.16}$$

where $\delta_0$ is the value measured when the surface normal is parallel to the incident beam direction. This can be explained by an increased path length of the incident beam electrons within the surface region if the beam/sample is tilted. In addition, $\delta$ is also dependent on the local curvature of the surface which determines the probability that a SE can escape. A region that possesses a positive radius of curvature, such as a region protruding from the surface, will enhance $\delta$, whereas regions with a negative radius of curvature will lead to a lower $\delta$ as the electrons will be trapped. Both dependencies – beam/sample tilt and local curvature – give rise to topological contrast in SE images.

The detector position also affects the number of SEs detected. When the incident beam direction is parallel to the surface normal, the same cosine dependency as for BSEs (Eq. 1.14) is observed; that is, the largest signal is detected when the detector is

placed parallel to the incident beam. This cosine dependency remains for large values of $\theta$, which contrasts with the strong anisotropy effect observed for BSEs.

## 1.2.3
### Auger Electrons (AEs)

When a high-energy electron excites an inner-shell electron to an unoccupied state above the Fermi level, the atom remains in an excited state. An empty inner-shell state exists which is subsequently filled by an electron from a higher state. During this relaxation process, a specific amount of energy is released that is used to generate characteristic X-rays; alternately, the energy can be transferred to an electron of the sample possessing a lower binding energy (see Figure 1.10). If the amount of energy transferred is large enough to excite this electron above the vacuum level, it can eventually leave the solid as a characteristic Auger electron, in what is termed a "nonradiative" process. These two possibilities are alternative processes by which the energy can be released. The probability whether X-ray generation or the emission of AEs dominate depends on the material. It is more likely that AEs are created for light elements, whereas for heavier elements the emission of X-rays is the dominant process. The AEs have a characteristic energy which is given by the difference of the binding energies of the electron states involved, and the work function of the material. Therefore, they can be seen as characteristic peaks in the electron yield versus electron energy curve (Figure 1.14); moreover, if an appropriate detector is used the AEs can be detected and quantified, so as to provide important information on the surface chemistry of the sample. Since AEs have energies comparable to SEs (they are, in fact, a type of secondary electron), their mean free path in the sample is extremely limited (1–2 nm). Although AEs contribute to the total SE signal acquired in SEM, specialized detectors for energy analysis – and thus the chemical analysis of AEs in SEM – are not often employed, as UHV and clean surfaces are required. As a result, modern AE systems are usually dedicated UHV scanning electron microscopes.

## 1.2.4
### Emission of Photons

### 1.2.4.1  Emission of X-Rays
As noted above, if an inner-shell electron (energy level $E_1$) has been excited to an unoccupied state above the Fermi level, the empty state can be filled with an electron from a higher state (energy level $E_2$), and the energy difference $\Delta E$ can be released by the (radiative) emission of X-rays with a characteristic energy (or wavelength) (see Figure 1.10). The wavelength can be calculated from the de Broglie relationship:

$$\lambda = \frac{hc}{\Delta E} \tag{1.17}$$

where $h$ is Planck's constant and $c$ is the speed of light. The transition from a higher level to the unoccupied inner-shell state is only allowed if the dipole selection rule is

fulfilled; that is, when the dipole moment number $l$ is changing by $\pm1$ (e.g., transitions form p-states to s-states are allowed while s-states to s-states are forbidden). If an unoccupied state in the K-shell is filled by an electron from the L-shell, the characteristic photon will contribute to the $K_\alpha$-line, if it is filled by an electron from the M-shell to the $K_\beta$ line, and so on. If the hole is in the L- or M-shell, then L and M characteristic radiation series will occur.

In addition to characteristic X-rays, the incident electron beam also generates X-ray radiation with a continuous energy distribution that ranges up to an energy equivalent to the total incident beam energy. When an electron passes through the Coulomb field of an atom it experiences a deceleration, which reduces the magnitude of the electron velocity. The energy released can be of any amount, and is emitted as electromagnetic radiation. Due to its origin such radiation is referred to as "Bremsstrahlung" or "braking radiation."

The escape depth of characteristic X-ray radiation depends on the interaction volume, and can be up to several micrometers in dimension; the escape depth for Bremsstrahlung is only slightly larger. The characteristic X-ray radiation can be used for quantitative chemical composition analysis where the nonlinear background in the X-ray spectrum, which stems from the Bremsstrahlung, must be removed prior to the analysis.

### 1.2.4.2  Emission of Visible Light

Besides electromagnetic radiation in the X-ray range, the emission of light can also be detected. The emission of photons in the visible range may occur due to different effects. For example, if a high-energy electron does not excite an inner-shell electron but rather a weakly bound valence electron, then the amount of energy released when the atom relaxes will be small. This process may lead to the emission of photons in the visible range (see Figure 1.10). In addition, X-rays generated in the solid by a high-energy electron can excite other atoms by themselves. The subsequent relaxation of these atoms may also lead to the emission of electromagnetic radiation in the visible or X-ray range; this process is termed "fluorescence."

### 1.2.5
### Interaction Volume and Resolution

Based on the above discussion on electron–matter interaction and the generation of the various signals, together with the volume of interaction, it is now possible to summarize some important points regarding the resolution capabilities of SEM. First, while its clear that the demagnification of an incident beam to as small a diameter as possible is important, the interaction volume, the escape depth of the signal of interest, and the type of detector each play critical roles in defining the resolution of the final image. Thus, unlike optical microscopy or TEM, it is not possible to define the resolution of the microscope alone, but rather the resolution of SEM for a particular sample investigated under specific operating conditions. As such, the main points defining the resolution for each particular signal available in SEM are worthy of summary.

### 1.2.5.1 **Secondary Electrons**

As noted above, the mean free path of SEs in solids is extremely limited, and consequently SEs generated far below the surface of the sample, either by the incident electrons or by BSEs, will not escape to the surface and reach the detector. If a conventional ET detector is used, then SEs generated by BSEs (SE2) will reach the detector, and the resolution will be defined by the interaction volume of BSEs reaching the surface of the sample (see Figure 1.13). The signal-to-noise ratio (SNR) of the image will depend on the yield of SEs and the detector position, but since the yield of SEs is always greater than 1.0, the SNR of SE images will usually be very good. This can be improved by increasing the current, and as a larger spot size will not significantly influence the backscattered-limited resolution, this is usually a good option if the SNR is important. For conducting specimens, a slower scan rate will also increase the SNR. This is especially important if the incident accelerating voltage of the electron beam is reduced in an attempt to limit the contribution of SE2, which will in turn decrease the SNR.

For FEG sources, the incident accelerating voltage can be reduced while maintaining a reasonable beam current, thus further reducing the contribution of the SE2 electrons. The use of an "in-lens" detector significantly reduces the contribution of SE2 electrons when operating at small working distances, thus improving the resolution of the image by using mainly SE1 electrons. A combination of a FEG source and "in-lens" detectors provides the definition of "high-resolution SEM."

### 1.2.5.2 **Backscattered Electrons**

As the mean free path of BSEs is significantly larger than that of SEs, it is the interaction volume with the sample which defines the resolution. "In-lens" detection systems operating at small working distances will improve the resolution by preventing BSEs from extended regions to reach the detector, but BSEs from the sample depth cannot be removed from the signal (Figure 1.13), and the SNR will always be limited due to the poor BSE yield compared to that of SEs. Reducing the accelerating voltage, and thus reducing the interaction volume (see Figure 1.11) is a good way of improving BSE resolution, bearing in mind the limited SNR. As the energy of the BSEs falls with the distance traversed in the sample, an energy-filtered BSE detector might improve the BSE resolution, and this is a possible direction for future SEM systems.

### 1.2.5.3 **X-Rays**

Since the mean free path of X-rays is significantly larger than that of electrons (due to a lower cross-section), the interaction volume within a specific material defines the resolution of X-ray images and the region for which the local concentration is measured (see Figure 1.13). One option would be to decrease the incident accelerating voltage, but only if it can be maintained at a value *greater* than the energy required for electron excitation and generation of a photon (in this case it will be necessary to know beforehand which elements are in the sample). In addition, while the interaction volume roughly defines the source of the X-rays (depending on the energy of the X-ray of interest), the fluorescence of X-rays can lead to a significantly larger volume of material from which X-rays are emitted.

The maximum depth in the sample from which the characteristic X-ray signal originates, ignoring fluorescence, can be approximated by:

$$Z_r \approx 0.033 \left( E_0^{1.7} - E_C^{1.7} \right) \left( \frac{\bar{A}}{\varrho \bar{Z}} \right) \tag{1.15}$$

where $\bar{A}$ and $\bar{Z}$ are the average atomic weight and average atomic number, respectively, in the volume of material being excited by the incident beam, $\varrho$ is the density, $E_0$ is the incident electron energy, and $E_C$ is the critical incident energy required for excitation. The maximum diameter of the excited volume generating the X-ray signal is usually approximated by:

$$D \approx \frac{0.231}{\varrho} \left( E_0^{1.5} - E_C^{1.5} \right). \tag{1.19}$$

## 1.3
## Contrast Mechanisms

### 1.3.1
### Topographic Contrast

From the discussion above, it follows that SE and BSE images may each show topographic contrast. The topographic contrast is mainly due to shadowing effects and to enhanced SE and BSE production at the edges and surface perturbations. Both effects are strongly affected by the angle of incidence of the primary electron and the position of the detector relative to the surface normal. Sample regions that are tilted towards the detector possess a much higher signal than those tilted away, giving rise to shadowing effects (Figure 1.17). In general, topographic contrast is usually associated with SE images, and this effect is strongly visible in images acquired
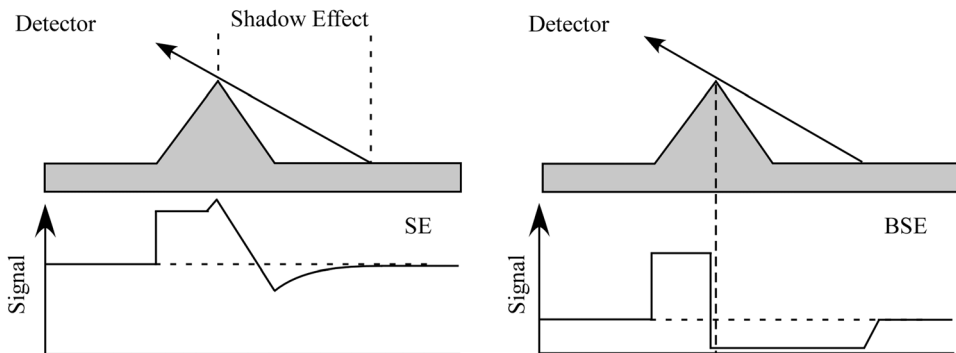


**Figure 1.17** Effect of local curvature and detector position on the SE and BSE signals. Only those electrons which are drawn with a solid line reach the detector. Modified after Ref. [8]

using an ET detector located at one side of the sample. For large surface perturbations (i.e., rough surfaces), the BSE signal in the region behind the topographic feature (relative to the detector position) is very low, as most generated BSEs do not reach the detector because their trajectories are basically unaffected by the applied bias (see Figure 1.17). This situation is different for the SEs, however, which are attracted and move towards the detector. Accordingly, the SE signal behind large surface perturbations will be higher than that of the BSE signal. As a result, low- to medium-magnification BSE images may have a stronger topographic contrast than SE images, if an off-axis detector is used. In general, images acquired using an ET detector appear as if the object is illuminated from one side, which results in a three-dimensional (3-D) effect (Figure 1.18). Some of this 3-D shadowing effect associated with the
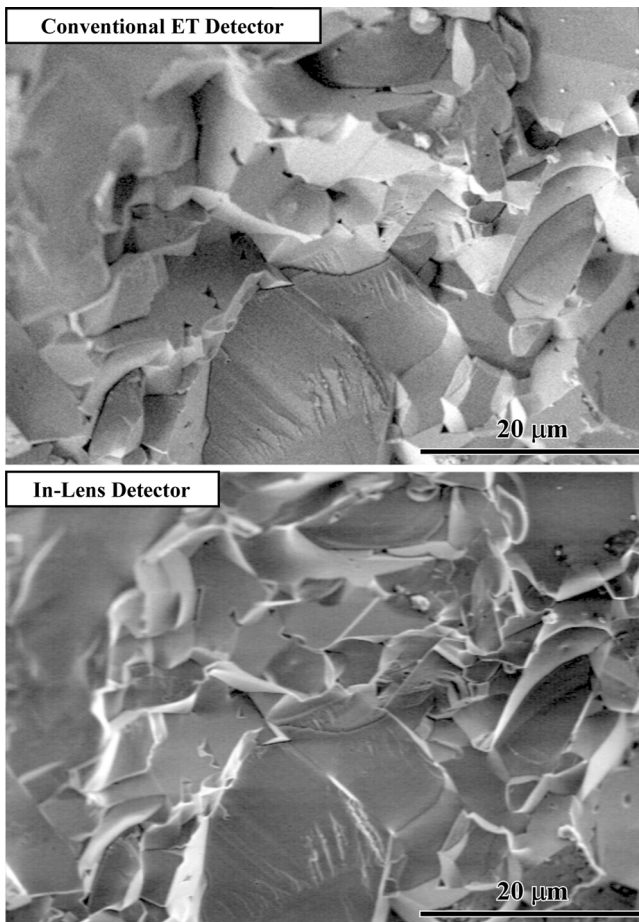


**Figure 1.18**   Comparison of SEM images taken with conventional detector and in-lens detectors. The SEM images show a fracture surface of alumina revealing cleavage facets and intergranular failure. Reproduced with permission from Ref. [4]; © 2008, John Wiley & Sons, 2008.)

surface topography is lost when using an in-lens detector located above the sample (Figure 1.18). In order to obtain topographic information with a segmented BSE detector, the signals of opposite sides of the sample must be subtracted, so as to enhance topographic contrast and reduce compositional contrast.

For high-magnification and small surface perturbations, SE images are superior in the topographic contrast and resolution compared to BSE images. This is due mainly to the escape depth, which is much larger for BSEs than for SEs, and results in a spatial resolution that is insufficient to differentiate between small surface topographic features in BSE images. When working with in-lens detectors registering only SE1 electrons, it is not only the depth resolution but also the lateral resolution that is strongly improved compared to BSE images. If a FEG is used in combination with an in-lens detector, then high-resolution imaging becomes possible (Figure 1.19). The resolution can be further improved to less than 1 nm when the microscope is operated at low accelerating voltages; this is a 10- to 20-fold improvement compared to the resolution obtained when using conventional SEM.

To summarize, the highest lateral resolution can be obtained by detecting SE1 using in-lens detectors and working at low incident accelerating voltages (low keV). Working at low keV can also be used to reduce charging. As can be seen in Figure 1.16, specific values exist (depending on the material) where the net current flow is zero; that is, the number of incident electrons is equal to the number of emitted electrons, which means that no net charge accumulates in the (nonconducting) sample, eliminating the need for conductive coatings (Figure 1.19).

Another point to mention here is the large depth-of-field in SEM, which allows for the imaging of large topographical changes, simultaneously. The large depth-of-field is due to the small angular aperture of the objective lens, and for large working distances is typically of the order of microns.
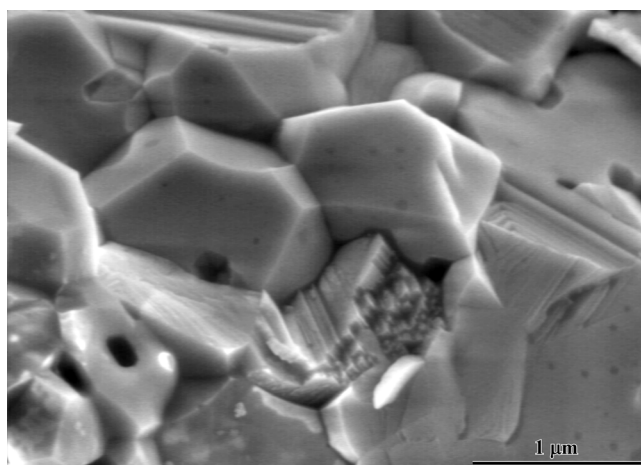


**Figure 1.19** SEM image of a fracture surface of alumina taken with an in-lens detector at 5 keV. Reproduced with permission from Ref. [4]; © 2008, John Wiley & Sons.

1.3.2
**Composition Contrast**

As discussed above, the BSE signal shows a much stronger dependence on the atomic number than does the SE signal. While the signal from BSEs is higher for phases with a high mean atomic number, SE images are often dominated by surface topographic contrast, leading to a less straightforward interpretation of the data (Figure 1.20). Consequently, BSE images are more often used to display the phase distribution in composite materials. Any remaining contribution of topographic contrast can be removed from BSE images if a segmented BSE detector is used, where the signals from opposite sides of the sample are added. Compositional contrast in SE images is usually only visible if topographic contrast contributions are small and any contamination layers or conductive layers are of no concern. That is, if the sample is pretreated by, for example, plasma cleaning, and when the microscope is operated at high vacuum levels and low accelerating voltages. Under these circumstances, the resolution in the SE images is much better than that of BSE images, due to the reasons mentioned above.

1.3.3
**Channeling Contrast**

Until now, the ways in which crystal orientation can influence the SE and BSE efficiency, and hence the contrast in the image, have not been discussed. Primary electrons can penetrate more deeply into the crystal along certain crystallographic orientations ("channeling"), compared to a random grain orientation. Accordingly, the efficiency ($\eta$) of BSE generation becomes lower when crystals are oriented in specific crystallographic orientations; in addition, the secondary electron yield $\delta$ is also reduced. The BSE and SE signals of such grains will be much lower than that of randomly oriented grains, leading to the so-called "channeling contrast." Usually, channeling contrast is visible only for clean surfaces – that is, in the absence of any contamination layers that would obscure this effect.

1.4
**Electron Backscattered Diffraction (EBSD)**

In addition to detecting the number of BSEs, it is also possible to acquire their diffraction patterns by using an electron backscattered diffraction (EBSD) detector. The EBSD system consists basically of a phosphorescent screen, a charge-coupled device (CCD) camera, a control unit to operate the scanning electron microscope and EBSD detector, and software to evaluate the acquired data. To obtain a high-intensity diffraction pattern, the sample is usually oriented such that the incident electron beam is tilted 70° relative to the surface normal. As noted above, this leads to an asymmetric angular distribution for the BSEs, with the highest intensity of diffuse scattering in the forward direction. The diffraction patterns obtained contain
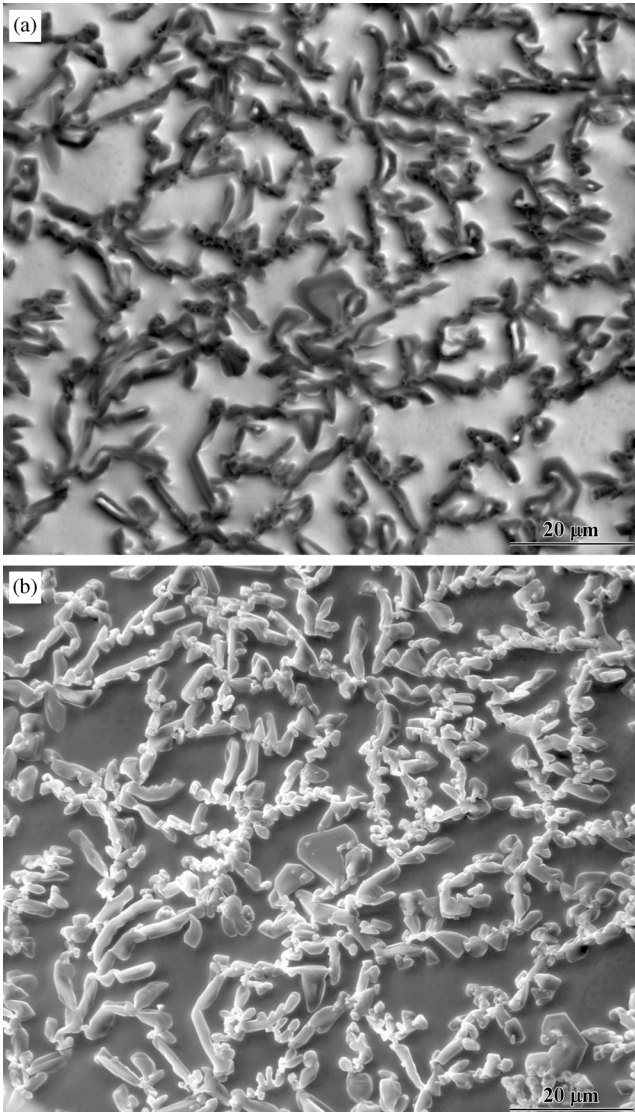
**Figure 1.20** (a) Back-scattered electron and (b) secondary electron SEM images of small $Al_2O_3$ particles on the surface of a nickel substrate. Reproduced with permission from Ref. [4]; © 2008, John Wiley & Sons.

important information relating to the local crystal structure and orientation, thus providing a new aspect to the more conventional morphological and elemental information acquired when using SEM.

The origin of the EBSD pattern is similar to that of Kikuchi patterns in TEM. The intensity distribution of the inelastically scattered electrons is diffuse, but with a maximum in the forward direction. Some of these diffusely scattered electrons fulfill

Bragg's law for a given set of crystallographic planes and are diffracted into certain directions. This will add intensity to the darker, high-angle scattering regions and reduce intensity in the low-angle scattering region – that is, closer to the forward direction. The diffracted beams lie on so-called Kossel cones with a half angle of $90°$-$\theta_B$ (where $\theta_B$ is the Bragg angle). The intersection of the Kossel cones with the plane of the detector are hyperbolae, but as all of the scattering angles are small the light and dark lines will appear straight and parallel. The distance between the lines is proportional to $2\theta_B$ and thus (for small angles) inversely proportional to the interplanar spacing. The EBSD pattern usually consists of several intersecting diffraction lines, each associated with a family of diffracting planes (Figure 1.21).

The EBSD pattern taken at one specific location can be used to obtain crystallographic information. For this, the EBSD patterns are calculated for various crystal structures and compared to the experimental data (Figure 1.21). In order to obtain
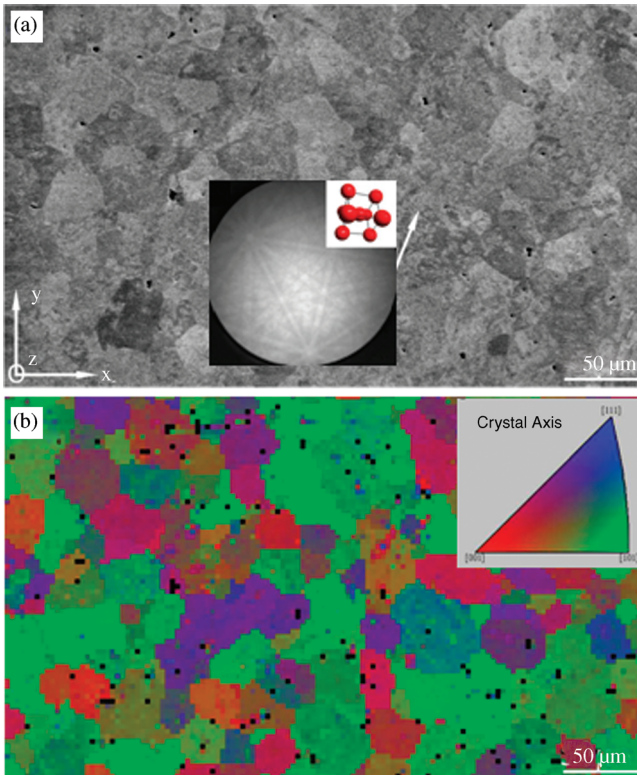


**Figure 1.21**   (a) Back-scattered electron image of a polycrystalline Tantalum wire with an EBSD pattern taken at the position marked by an arrow and corresponding crystal orientation; (b) Orientation map and corresponding color coding. Figures reproduced from S. Mayer, S. Pölzl, G. Hawranek, M. Bischof, C. Scheu, and H. Clemens (eds) (2006) Metallographic Preparation of Doped Tantalum for Microstructural Examinations using Optical and Scanning Electron Microscopy, in *Practical Metallography*, Vol. 43, No. 12, pp. 614–628.

orientation distribution maps, this procedure is repeated as a function of position across the sample surface during incident beam irradiation. After having evaluated the data, the results can be color-coded for selected ranges of crystal orientation (or phase). A prerequisite for the successful application of orientation imaging microscopy using SEM is a high-quality crystalline surface with minimal surface contamination, since both will affect the quality of the EBSD pattern.

## 1.5
## Dispersive X-Ray Spectroscopy

The generated X-rays can be detected by using either an energy dispersive spectrometer (EDS) or a wavelength dispersive spectrometer (WDS). EDS is based on a solid-state detector that is a cryogenically cooled, negatively biased *p-i(intrinsic)-n* semiconductor diode. The incoming X-rays produce electron-hole pairs that are separated in the electrical field of the diode; this leads to a current pulse that can be converted to a voltage pulse which is then electronically amplified, digitized, and counted in a multichannel analyzer. The electrical charge generated is proportional to the energy of the incoming X-rays, and accordingly these are discriminated by their energies. The EDS detector is protected against contamination from the microscope by a thin window. Depending on the type of window used, elements with $Z > 5$ (boron) or $Z > 11$ (sodium) can be detected. Unfortunately, low-energy X-rays can be easily absorbed in the detector, leading to errors in quantitative analysis.

Consequently, for the analysis of light elements it is beneficial to use a WDS system. In this type of spectrometer, which is based on a curved crystal diffractometer, only those X-rays which fulfill Bragg's law for a specific orientation of the detector crystal are counted, and accordingly they are discriminated by their wavelengths. Due to the geometric discrimination, all characteristic X-ray peaks must be scanned sequentially. If several peaks are to be collected at a time, then several spectrometers must be used simultaneously (or extended acquisition times will be required). The detection of X-rays according to their wavelength has another major advantage compared to energy-dispersive systems, in that the energy resolution is at least an order of magnitude better than EDS. This is important if peak overlap inhibits identification and quantification. The disadvantage of the WDS is the much longer data collection time that is associated with the sequential acquisitions, compared to the parallel data collection mode used in the EDS.

As described above, in addition to the identification of elements present in a specimen, characteristic X-rays can also be used for chemical composition analysis. A semi-quantitative analysis can be performed by applying the following equation:

$$\frac{C_i}{C_{(i)}} = ZAF \frac{I_i}{I_{(i)}}. \tag{1.20}$$

where $C_i$ and $C_{(i)}$ are the concentration of species $i$ in the unknown compound/specimen and in a pure standard, respectively, and $I_i$ and $I_{(i)}$ are the intensities (number of counts) of the corresponding X-ray peaks after background subtraction.

The included *ZAF* correction represents the atomic number effects (*Z*), absorption (*A*) and fluorescence (*F*) which must be taken into account for bulk specimens. The background caused by the Bremsstrahlung can either be fitted by linear interpolation or calculated using a theoretical model (Kramers relation), and is then subtracted from the original data to obtain the net signal necessary for the quantification.

Several approaches may be employed to acquire X-ray data in SEM (Figure 1.22). In order to obtain the chemical composition of a specific location, the electron beam can be placed stationary on a sample position (point analysis). If contamination occurs, or if an average chemical composition analysis is of interest, the EDS spectrum can also be acquired while the electron beam is scanning over a certain area (area measurements). To determine the chemical composition across, for example, an interface, line-scans are often acquired (Figure 1.22). In this mode, the electron beam is scanned across a chosen line, and at specific points of this line either a complete spectrum is acquired or the intensity of individual, selected X-ray energies is measured. The latter measurement has the advantage of shorter acquisition times, with typical acquisition times of approximately 100 s for a complete spectrum being reduced by a factor of five, or more. However, this type of measurement permits only semi-quantitative analysis, and can only be used to display the intensity distribution
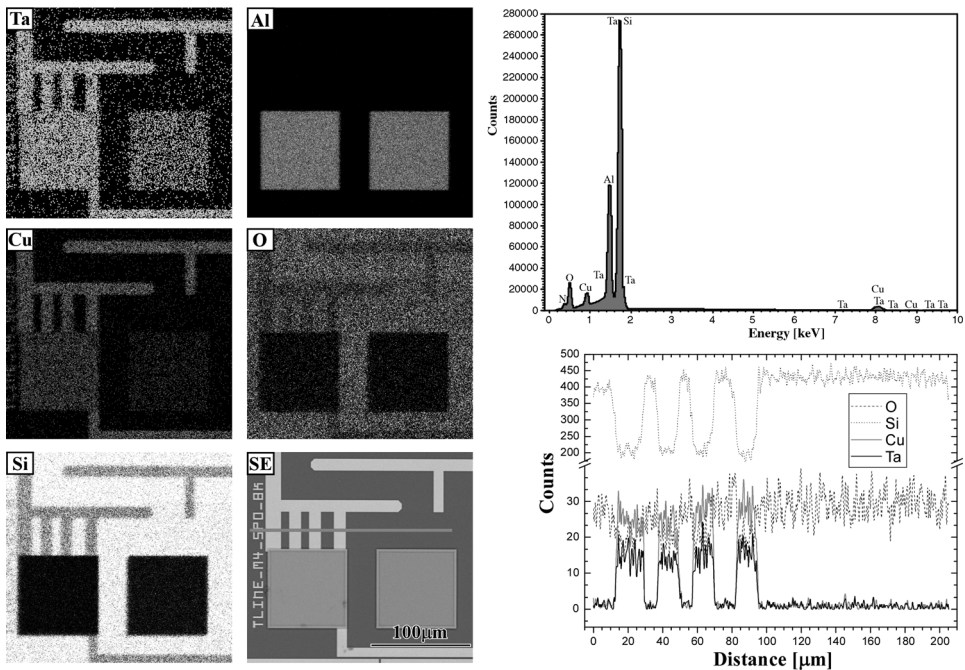


**Figure 1.22** SEM image and corresponding X-ray dot images revealing the elemental distribution of Ta, Al, Cu, O and Si of a electronic device. At the right upper side is displayed an EDS spectrum taken at a specific point of the device. At the right lower side are shown the results obtained with a line scan measurement. Reproduced with permission from Ref. [4]; © 2008, John Wiley & Sons.

of the chosen elements. The acquisition of EDS data or chosen X-ray energy regions along a certain raster can be used to display the elemental distribution of specific sample areas (Figure 1.22). The corresponding X-ray dot images/elemental maps are then used to investigate the distribution of various phases within the sample (Figure 1.22). Together with the information obtained by BSE or SE images, these provide valuable information for materials scientists and engineers. However, from the above discussion it should be clear that the X-ray signal stems from an interaction volume that is much larger than the electron beam size used for the data acquisition.

## 1.6
## Other Signals

As noted above, the interaction of the incident beam with an optically active material can lead to the emission of light. This cathodoluminescence (CL) can be detected by using a special detector that consists of a semi-ellipsoidal mirror for light collection and focusing, a light guide, and a photomultiplier. The wavelength of the emitted light depends on the composition and structure, and thus can be used to probe local changes of these microstructural features when the beam is scanned across the sample. At low temperatures, the wavelength distribution becomes very narrow and typically shows a pronounced maximum at the energy associated with the bandgap in semiconductors and isolators. Accordingly, local changes in bandgap and impurity states can be investigated. As CL is generated within the interaction volume, the spatial resolution is much worse than when acquiring BSE or SE images. Moreover, CL is very sensitive to low impurity levels (0.01 ppm) and, as such, much more sensitive than EDS.

Other alternative imaging modes are related to electron beam-induced current (EBIC) or electron beam-induced voltage (EBIV). These are useful when studying defects and structures in semiconductor devices, as the incident electron beam can be used to create electron-hole pairs in a semiconductor that can be separated with either an internal (e.g., *pn-* junction) or external electrical field. By measuring either the associated voltage (EBIV mode) or current (EBIC mode) while scanning the beam across the area of interest, it is possible to image local changes in the electronic properties.

## 1.7
## Summary

In this chapter, the main components of the scanning electron microscope and the image formation process have been described. The important parameters that limit the resolution – primarily the incident electron beam diameter and the interaction volume in the sample – have been discussed in detail. The escape depth which governs the lateral and depth resolution depends on the type of signal to be used for imaging, and is different for SE1 and SE2 electrons, BSEs, X-rays, and light. How the

contrast in SE and BSE images can be interpreted in terms of topology and composition variations has also been discussed, and the effect of beam tilt, detector position and channeling on the image contrast described. The analytical tools available for SEM to determine the chemical composition (via EDS and WDS) and the crystallographic orientation (EBSD), as well as the detection of other signals characteristic of the material being studied (e.g., CL, generated current and voltage) have also been outlined. In summary, modern SEM and its associated analytical tools provide unique possibilities for materials characterization. Notably, due to the simplicity of its use and its high resolution, SEM is also very well suited to *in-situ* studies.

## References

1 Reimer, L. (1998) *Scanning Electron Microscopy: Physics of Image Formation and Microanalysis*, 2nd edn, Springer Verlag, Berlin, Heidelberg, New York; Germany and USA.

2 Goodhew, P.J., Humphreys, J. and Beanland, R. (2001) *Electron Microscopy and Analysis;*, 3rd edn, Taylor & Francis, London, New York.

3 Goldstein, J., Newbury, D., Joy, D., Lyman, C., Echlin, P., Lifshin, E., Sawyer, L., and Michael, J. (2003) *Scanning Electron Microscopy and X-Ray Microanalysis*, 3rd edn, Springer, New York.

4 Brandon, D. and Kaplan, W.D. (2008) *Microstructural Characterization of Materials*, 2nd edn, John Wiley & Sons, West Sussex, UK.

5 Joy, D.C., Romig, A.D. and Goldstein, J.I. (eds) (1986) *Principles of Analytical Electron Microscopy*, Plenum Press, New York, London.

6 Egerton, R.F. (1996) *Electron Energy-Loss Spectroscopy in the Electron Microscope*, 2nd edn, Plenum Press, New York.

7 Drouin, D., Couture, A.R., Joly, D., Tastet, X., Aimez, V., and Gauvin, R. (2007) CASINO V2.42 – A fast and easy-to-use modeling tool for scanning electron microscopy and microanalysis users. *Scanning*, **29** (3), 92–101.

8 Reimer, L. and Pfefferkorn, G. (1977) *Rasterelekronenmikroskopie*, Springer-Verlag, Berlin, Heidelberg, New York.